


Nonrelativistic spin splittings and altermagnetism in twisted bilayers of centrosymmetric antiferromagnets

Sajjan Sheoran^{✉*} and Saswata Bhattacharya^{✉†}

Department of Physics, Indian Institute of Technology Delhi, New Delhi 110016, India

 (Received 17 January 2024; accepted 30 April 2024; published 15 May 2024)

Magnetism-driven nonrelativistic spin splittings (NRSS) are promising for highly efficient spintronics applications. Although 2D centrosymmetric (in four-dimensional spacetime) antiferromagnets are abundant, they have not received extensive research attention owing to symmetry-forbidden spin polarization and magnetization. Here, we demonstrate a paradigm to harness NRSS by twisting the bilayer of centrosymmetric antiferromagnets with commensurate twist angles. We observe *i*-wave altermagnetic spin-momentum coupling by first-principles simulations and symmetry analysis on prototypical MnPSe₃ and MnSe antiferromagnets. The strength of NRSS (up to 80 meV Å) induced by twisting is comparable to SOC-induced linear Rashba-Dresselhaus effects. The results also demonstrate how applying biaxial strain and a vertical electric field tune the NRSS. The findings reveal the untapped potential of centrosymmetric antiferromagnets and thus expand the material's horizons in spintronics.

DOI: [10.1103/PhysRevMaterials.8.L051401](https://doi.org/10.1103/PhysRevMaterials.8.L051401)

Spin splittings in the electronic structure of crystalline solids play a pivotal role in spintronics applications (e.g., spin transistor) [1,2]. The conventional spin-orbit coupling (SOC) induced Rashba-Dresselhaus [3–6] in nonmagnetic and Zeeman effects in ferromagnetic (FM) materials create spin splittings under certain crystalline (i.e., inversion [\mathcal{P}]) and time-reversal symmetry (\mathcal{T}) breaking [7], respectively. SOC-induced spin splitting and the resulting spin polarization engender spin-orbit torques [8], while FM spin polarization has been widely known for spin generation and detection [1]. However, the SOC effect introduces spin dephasing mechanisms [9–11], limiting the practical application. In addition, materials with heavy elements having significant SOC impart additional challenges, including scarcity, toxicity, and instability. Therefore, nonrelativistic spin splitting (NRSS) is an important avenue to pursue.

Recently, antiferromagnetic (AFM) materials have emerged as viable substitutes for nonmagnetic and FM materials, benefiting from resilience toward stray fields, ultrafast dynamics, and magnetotransport effects [12–16]. The coupling of spin to lattice degrees of freedom via a staggered collinear compensated magnetism leads to alternating NRSS, termed altermagnetism [17–19]. Numerous efforts have been undertaken to investigate NRSS in AFM materials by breaking combined $\mathcal{PT}\tau$ and/or $U\tau$ symmetries, where U and τ are spinor and translation symmetry, respectively [20–26]. Nevertheless, the majority of AFM spin splittings are limited to bulk materials (e.g., MnF₂ [21,27], LaMnO₃, and MnTiO₃ [23]), require SOC (e.g., MnS₂ [23] and ZnV₂O₄ [28]), or external perturbation [29–31].

Since the experimental revelation of 2D magnetic ordering, 2D van der Waals (vdW) magnetic materials have

garnered significant attention in scientific research, emerging as promising contenders for future information technology. Interestingly, two recent works focus on spin splitting in FM NiCl₂ [32] and FeBr₂ (although “hidden”) [33] monolayers vdW stacked antiferromagnetically. In contrast, antiferromagnetism-induced spin splitting among centrosymmetric materials with AFM order within each layer is not achieved due to \mathcal{PT} symmetry-enforced spin degeneracy. Despite being abundant in nature, this impedes practical applications of 2D centrosymmetric AFM materials [34–38].

This study generates NRSS and altermagnetism in \mathcal{PT} symmetric AFM monolayers vdW stacked with a relative twist. We perform density functional theory (DFT) simulations on twisted bilayer (tb-) MnPSe₃ and MnSe as prototypical candidates. The *i*-wave spin-momentum coupling arises in the 2D Brillouin zone (BZ) for θ ($\neq 0^\circ, 60^\circ$) tb-MnPSe₃ and MnSe. Based on the symmetry analysis, we find that the strengths of NRSS along specific k paths are comparable to the conventional SOC-induced Rashba-Dresselhaus effects. Moreover, external perturbations (i.e., electric and strain fields) provide exceptional tunability to NRSS.

MnPSe₃ and MnSe (space group No. 162, $P\bar{3}1m$) represent two distinct classes of vdW materials that possess exceptional exfoliation properties [34–38]. Unlike the majority of other 2D magnetic materials, they exhibit an AFM arrangement, conforming to the conventional collinear Néel order on the honeycomb lattice (Fig. 1). This in-plane antiferromagnetism is different from the A-type antiferromagnetism observed in various other 2D vdW compounds, i.e., MnBi₂Te₄ [39], CrI₃ [40], and CrSBr [41], where individual layers exhibit FM order but stack antiferromagnetically. The antiferromagnetism of MnPSe₃ is “truly” in-plane and differs from that of MnSe, where Mn ions with opposite magnetic moments (Mn_A and Mn_B) form unusual out-of-plane ordering within the individual layer. Note that the orientation of on-site magnetic moments concerning the lattice only matters if SOC

*phz198687@physics.iitd.ac.in

†saswata@physics.iitd.ac.in

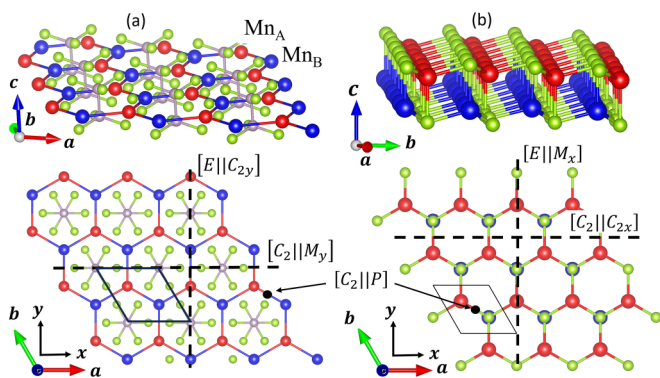


FIG. 1. Crystal structure of the monolayer (a) MnPSe_3 and (b) MnSe . The red and blue spheres indicate Mn atoms with the opposite collinear magnetic densities. The brown and green spheres represent P and Se atoms, respectively. The Cartesian (x, y, z) coordinate system and the hexagonal unit cell (with solid black lines) are shown for each case. The nontrivial spin-group symmetries are also highlighted. E and C_2 represent identity and twofold rotation (about an axis perpendicular to spins) in spin space, respectively. \mathcal{M}_i and C_{2j} denote the mirror reflection perpendicular to the i axis and the twofold rotation parallel to the j axis in real space, respectively. \mathcal{P} represents the real-space inversion.

is included. Therefore, nonrelativistic spin-group formalism is described for the symmetry transformations in decoupled real and spin space [18,42–45]. The spin-symmetry operations $[R_i||R_j]$ of monolayer MnPSe_3 and MnSe are indicated in Fig. 1, where the transformation on the left (right) of the double vertical bar acts on the only spin (real) space. In addition, collinear magnets always have additional symmetry $[\bar{C}_2||\mathcal{T}]$ arising from spin-only groups, where \bar{C}_2 is the twofold rotation perpendicular to the collinear spin axis, followed by spin-space inversion. Mn_A and Mn_B sublattices are connected through $[C_2||\mathcal{P}]$ symmetry in monolayer MnPSe_3 and MnSe . $[C_2||\mathcal{P}][\bar{C}_2||\mathcal{T}]$ ($\equiv \mathcal{PT}^{-1}$) symmetry transforms energy eigenstate $E(k, \sigma)$ as $[C_2||\mathcal{P}][\bar{C}_2||\mathcal{T}]E(k, \sigma) = [C_2||\mathcal{P}]E(-k, \sigma) = E(k, -\sigma)$, leading to spin degeneracy throughout the Brillouin zone (BZ). We have verified that through DFT + U calculations performed on the projector augmented wave method [46] based VASP [47] code (methods are detailed in Sec. I of the Supplemental Material (SM) [48]). DFT simulated energy bands for monolayer MnPSe_3 and MnSe are doubly degenerate (see Sec. II in the SM [48]). The semiconducting MnPSe_3 and MnSe have a magnetic moment of $\sim 4.5 \mu_B/\text{Mn}$ with weak interlayer coupling. In addition, $[C_2||\tau]$ can also enforce spin degeneracy by connecting opposite spin sublattices by translation (τ) as $[C_2||\tau]E(k, \sigma) = E(k, -\sigma)$. Since 2D systems have only in-plane components of momentum k_{\parallel} , nonrelativistic Hamiltonians for 2D systems may have symmetries other than $[C_2||\mathcal{P}]$ and $[C_2||\tau]$ enforcing spin degeneracy. For example, $[C_2||\mathcal{M}_z]$ symmetry also enforces spin degeneracy throughout the BZ in 2D materials, with $\mathcal{M}_z : \mathcal{M}_z k_{\parallel} = k_{\parallel}$ as a planar mirror reflection (see Sec. II of the SM [48] for details). That

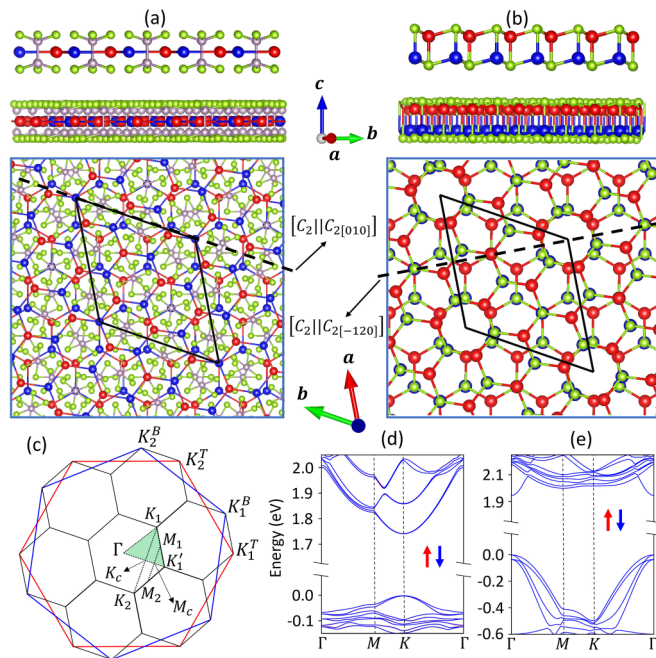


FIG. 2. The moiré superlattices formed by twisting bilayer of (a) MnPSe_3 and (b) MnSe by 21.79° . (c) The moiré BZ construction uses BZs of the top and bottom layers. The large red and blue hexagons are the first BZ of the top and bottom layers, respectively, and black hexagons represent the BZ corresponding to the moiré superlattice. Spin-polarized band structure of (d) tb- MnPSe_3 and (e) tb- MnSe at the PBE level. The red and blue bands denote spin-up and spin-down states, respectively.

makes achieving NRSS even more difficult for 2D materials. In the case of MnPSe_3 and MnSe monolayers, $[C_2||\mathcal{M}_z]$ is already broken [Figs. 1(a) and 1(b)], whereas the type-III Shubnikov magnetic space group (MSG) ensures $[C_2||\tau]$ symmetry breaking [49]. The only symmetry-preserving spin degeneracy is $[C_2||\mathcal{P}]$ symmetry in monolayers MnPSe_3 and MnSe .

Bilayer MnSe and MnPSe_3 are obtained from monolayers with various high-symmetry stackings as used in Ref. [30]. Spin-up and spin-down states are degenerate for AA, AA', AB, and BA stackings (see Sec. II of the SM [48]). The $[C_2||\mathcal{P}]$ symmetry enforces double degeneracy in AA, AB, and BA, whereas double degeneracy in AA' stacking is protected by the $[C_2||\mathcal{M}_z]$. Therefore, high-symmetry stackings are not an ideal for SOC-unrelated spin splitting in 2D \mathcal{PT} -symmetric antiferromagnets.

Commensurate twisted bilayers are obtained using coincidence lattice theory [50] by taking the AA bilayer as the untwisted limit to break \mathcal{PT} symmetry. A periodic lattice structure, including the moiré superlattice, can form with special twist angle θ , $\cos \theta = \frac{n^2 + 4mn + m^2}{2(m^2 + mn + n^2)}$, where m and n are whole numbers [51]. We only considered twist angles that resulted in reasonably sized commensurate supercells with the number of atoms per unit cell fewer than 350. Figures 2(a) and 2(b) show relaxed crystal structures and moiré patterns in $\theta = 21.79^\circ$ tb- MnPSe_3 and tb- MnSe [see moiré BZ in Fig. 2(c)]. Different possible interlayer and intralayer magnetic couplings $\uparrow\uparrow\uparrow\uparrow$,

¹Therefore, we use “[$C_2||\mathcal{P}$]” and “ \mathcal{PT} ” interchangeably.

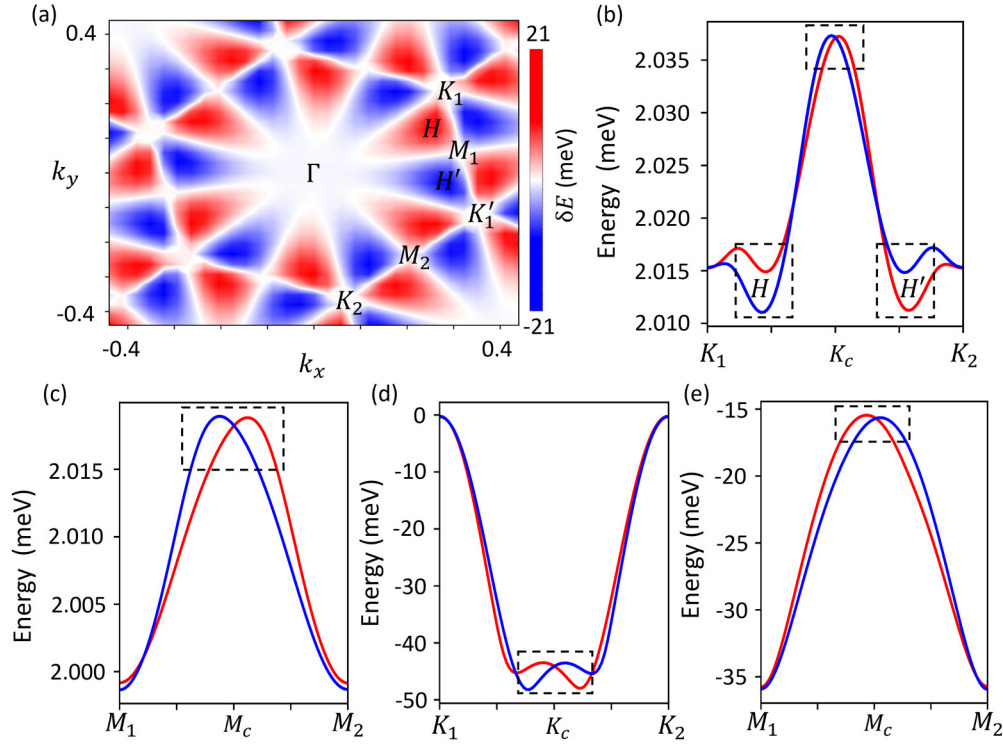


FIG. 3. (a) Spin splitting energy [$\delta E = E_{\uparrow}(k) - E_{\downarrow}(k)$] distribution of valence band in 21.79° tb-MnSe. The units of k_x and k_y are \AA^{-1} . Conduction bands of tb-MnSe along the (b) K_1 - K_c - K_2 and (c) M_1 - M_c - M_2 paths [see Fig. 2(c) for paths]. Valence bands of tb-MnPSe₃ along the (d) K_1 - K_c - K_2 and (e) M_1 - M_c - M_2 paths. The red and blue curves denote spin-up and spin-down bands, respectively. Black dashed squares represent prominent spin splittings. Fermi energy is set to valence band maximum.

$\uparrow\downarrow\uparrow\downarrow$, $\uparrow\downarrow\downarrow\uparrow$, and $\uparrow\uparrow\downarrow\downarrow$ were considered to determine the preferred magnetic ordering (here, up and down arrows represent the relative magnetic moment direction on Mn atoms). The most stable magnetic structure is $\uparrow\downarrow\uparrow\downarrow$, where magnetic order is intralayer and interlayer AFM [Figs. 2(a) and 2(b)]. Twist angle leads to small variation in the magnitude of local magnetic moments from 4.441 to 4.448 μ_B/Mn in tb-MnSe. The tb-MnPSe₃ and tb-MnSe are altermagnetic with opposite spin sublattices connected through the rotation symmetries [$C_2||C_{2[010]}$] and [$C_2||C_{2[-120]}$], respectively) with net zero magnetization [Figs. 2(a) and 2(b)]. In addition to Mn atoms, nonmagnetic ligands also contribute to \mathcal{PT} -symmetry breaking in tb-MnPSe₃ and tb-MnSe.

First, we compute the spin-polarized band structures of tb-MnPSe₃ and tb-MnSe along the high-symmetry paths (HSPs) [Figs. 2(d) and 2(e)]. The bands are spin degenerate along HSPs due to special symmetries arising at arbitrary k points on the HSP. For instance, [$C_2||C_{2[010]}$] in tb-MnPSe₃ transforms the spin-up to the spin-down state along the Γ - K path, enforcing degeneracy between them (see Sec. III of the SM [48]). However, this is not the case for any generic k point. No symmetry transforms spin-up to spin-down at the generic k point, leading to the lifting of the Kramers degeneracy. Therefore, the full BZ analysis of spin splitting is required. We plot spin-splitting energy δE [$= E_{\uparrow}(k) - E_{\downarrow}(k)$] of valence bands in tb-MnSe as a function of k [Fig. 3(a)]. The δE is invariant under real-space inversion [$\delta E(k) = \delta E(-k)$] due to spin-only symmetry [$C_2||T$], which transforms energy eigenstates [$C_2||T$] $E(k, \sigma) = E(-k, \sigma)$. Additionally, [$C_2||T$], along with [$E||C_{3z}$], leads to sixfold-

symmetric ($[E||C_{6c}]$) planar i -wave spin-momentum coupling, which is different from the threefold symmetry of SOC-induced δE observed in well-known monolayer MoS₂ [52]. Similar patterns are also observed for δE of the conduction band (CB) in tb-MnSe and valence band (VB) in tb-MnPSe₃ (see Sec. III in the SM). The maximum NRSS is observed at the orthocenter (H/H') of the triangle formed by Γ , M , and K_1/K'_1 points. Maximum splitting observed is 20.4, 4.2, and 5.1 meV for the VB of tb-MnSe, CB of tb-MnSe, and VB of tb-MnPSe₃, respectively. Maximum δE is smaller than well-known bulk antiferromagnets, i.e., MnF₂ [21], Fe₂TeO₆ [31], and LaMnO₃ [23]. The δE observed in the CB of tb-MnPSe₃ is negligible and beyond the accuracy of our calculations.

To understand the nature of NRSS, we plot band structures along both K_1 - K_c - K_2 and M_1 - M_c - M_2 directions [Figs. 3(b)–3(e)]. Interestingly, linear NRSS is observed around K_c and M_c for the VB and CB of tb-MnSe and VB of tb-MnPSe₃. The spin splittings exhibit contrasting characteristics at the H and H' points, featuring distinct valleys and maximum strength, suggesting the potential for valleytronics applications in twisted bilayers of antiferromagnets [53,54]. Note that the spin splittings around the Γ point, along the Γ - H/H' direction, exhibit cubic characteristics, which result in their being relatively small and, as such, are excluded from the current discussion [55]. Spin splittings around the M_c and K_c points are further analyzed using the symmetry-based model Hamiltonian, deduced using the “method of invariants” [55,56]. The symmetry element (besides identity) of the M_c/K_c point is [$C_2||C_{2[010]}$] and [$C_2||C_{2[-120]}$] for tb-MnPSe₃ and tb-MnSe, respectively [see Figs. 2(a) and 2(b)]. The symmetry-invariant

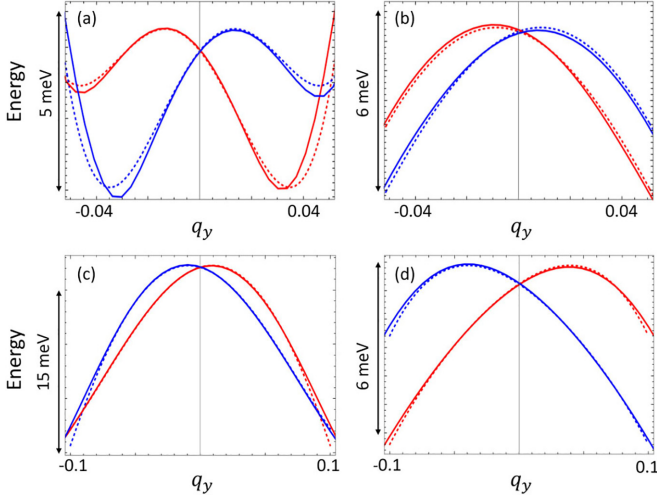


FIG. 4. Valence bands of tb-MnPSe₃ around (a) K_c and (b) M_c along q_y direction. (c) and (d) are counterparts of (a) and (b), respectively, obtained for conduction bands of tb-MnSe. The solid and dotted lines are bands obtained from DFT and the model described by Eq. (1), respectively.

terms include $\alpha q_{y'} \sigma_z$ and $q_{y'} q_{i'}^2 \sigma_z$ ($i = x', y'$), where $q = k - M_c/K_c$ are the momenta measured from M_c/K_c (see Sec. III of the SM [48] for notation, derivation, and discussion). Therefore, splitting is absent along the $q_{x'}$ ($K_c-K'_1$ and $M_c-K'_1$) direction, whereas it is present along the $q_{y'}$ direction ($K_c-K_{1/2}$ and $M_c-M_{1/2}$). To understand the NRSS along the $q_{y'}$ direction, it is possible to write an effective Hamiltonian (H_{eff}), up to third order in k :

$$H_{eff} = \alpha q_{y'} \sigma_z + \eta q_{y'}^3 \sigma_z. \quad (1)$$

Here, α and η are the constants determining the strength of NRSS. The primary linear term in Eq. (1) leads to the linear splitting of spin-up and spin-down energy bands around the M_c and K_c points, similar to the linearly split bands by SOC-induced Rashba-Dresselhaus effect. Note that spin splitting in Eq. (1) originates from altermagnetic ordering and is completely nonrelativistic. On the other hand, the Rashba-Dresselhaus effect is induced by the spin-orbit field originating from noncentrosymmetric sites and is of relativistic origin. We fit the energy levels around M_c and K_c along the q_y direction to obtain spin-splitting parameters. The fits are obtained by minimization of the summation, $S = \sum_{i=1}^2 \sum_q f(q) |\text{Det}[H_{eff}(q) - E^i(q)I]|^2$ over the i th energy

eigenvalues $[E^i(q)]$ as training sets. We have also included a weight function $f(q)$ with normal distribution to get a better fit near the spin-degenerate point and avoid overfitting. The obtained fits to the DFT energy levels of tb-MnPSe₃ and tb-MnSe are shown in Figs. 4(a)–4(d). The Hamiltonian in Eq. (1) with $\alpha = 58.6$ meV Å and $\eta = 34.2$ eV Å³ provides the best fit to the VBs of tb-MnPSe₃ around the K_c point [Fig. 4(a)], whereas $\alpha = 39.8$ meV Å and $\eta = 3.5$ eV Å³ are observed for VBs of tb-MnPSe₃ around the M_c point, respectively [Fig. 4(b)]. Similarly, a linear splitting strength of 35.4 and 60.7 meV Å is observed in CBs of tb-MnSe around the K_c and M_c points, respectively [Figs. 4(c) and 4(d)]. The NRSS is comparable to those experimentally reported in the literature (e.g., 10 meV Å for KTaO₃ [57], 4.3 meV Å for LaAlO₃/SrTiO₃ interface [58], ~70 meV Å in InGaAs/InAlAs interface [59], and 77 meV Å for MoS₂ monolayer [60]). The growing field of twistrionics makes NRSS observed in tb-MnPSe₃ and tb-MnSe experimentally accessible.

The 2D magnetic materials can be classified into five prototypes depending on the magnetic order, MSG, and whether NRSS is absent or present in a monolayer (Table I). Spin degeneracy in nonmagnetic materials (SST-1) is enforced by $[C_2||E]$ and remains preserved under twisting operations. In contrast, FM materials (SST-2) show NRSS in both monolayer limits and two layers stacked antiferromagnetically with a twist [32]. Altermagnetic materials (SST-4) have opposite-spin sublattices connected through mirror-rotation symmetries with opposite-spin electronic states separated in the momentum space. MSG type IV always has AFM order with $[C_2||\tau]$ symmetry (SST-5) and necessitates SOC to induce spin splitting [23]. 2D AFM materials with MSG type III containing $[C_2||\mathcal{P}]$ (\mathcal{PT}) or $[C_2||\mathcal{M}_z]$ (SST-3) are unique, as NRSS is absent in the monolayer and presented in twisted bilayer. Therefore, the twisting operation generates splittings in SST-3 type materials, the most common magnetic ordering found in nature.

Although controlling crystal symmetries in bulk materials is challenging, it has been shown that gating can effectively break the symmetries in 2D materials, including twisted bilayers [61–63]. In the following, we apply an out-of-plane electric field (\mathcal{E}_z) to the tb-MnPSe₃ and tb-MnSe in DFT simulations self-consistently using the approach introduced by Neugebauer and Scheffler [64]. The electric field creates not only polarization but also magnetization by breaking opposite spin-sublattice transformation through the magnetoelectric coupling [65]. The Zeeman-like Hamiltonian under \mathcal{E}_z is given

TABLE I. Classification of 2D materials based on the MSG type, magnetic order, and their impact on the NRSS. The relevant spin-group symmetry is also indicated in the case of spin degeneracy at generic k .

Spin-splitting prototype	Monolayer			Twisted bilayer		Examples
	Magnetic order	MSG type	NRSS at generic k	NRSS at generic k		
SST-1	Nonmagnetic	II	$\times([C_2 E])$	$\times([C_2 E])$	MoS ₂ [67], PtSe ₂ [68]	
SST-2	Ferromagnetic	I/III	✓	✓	NiCl ₂ , CrI ₃ , CrN, CrSBr [32]	
SST-3	Antiferromagnetic	III	$\times([C_2 \mathcal{P}]/[C_2 \mathcal{M}_z])$	✓	MnPSe ₃ , MnSe (this work)	
SST-4	Altermagnetic	I/III	✓			
SST-5	Antiferromagnetic	IV	$\times([C_2 \tau])$			

by [31], $\hat{H}_Z = \lambda \mathcal{E}_z \sigma_z$, where λ is a coefficient determining coupling strength. In the presence of \mathcal{E}_z , the spin-degenerate levels at the high-symmetry points (Γ , M , and K) and along HSPs will be split into two sublevels, $E_+ = \lambda \mathcal{E}_z$ and $E_- = -\lambda \mathcal{E}_z$ [Figs. 5(a)–5(c)]. We observe that the splitting induced by \mathcal{E}_z in tb-MnPSe₃ and tb-MnSe exhibits markedly distinct characteristics. Specifically, an electric field \mathcal{E}_z with a strength of 10 MV/cm results in nearly negligible splitting at the Γ point for tb-MnPSe₃, suggesting a small λ [Figs. 5(a) and 5(c)]. In contrast, for tb-MnSe, the Γ point experiences a significantly larger Zeeman-type splitting (~ 175 meV) induced by an electric field \mathcal{E}_z of 10 MV/cm [Figs. 5(b) and 5(c)]. This disparity can be explained through structural analysis: in tb-MnPSe₃, Mn atoms with opposite magnetic moments lie within the same z plane, while in tb-MnSe, they are situated in different z planes, thus supporting magnetoelectric coupling when an electric field is applied along the z direction. On the contrary, when we compare the Zeeman splittings induced in the CB and VB of tb-MnSe at the Γ point [Fig. 5(b)], it becomes evident that the splitting in the VB is significantly greater in magnitude compared to that in the CB. This pronounced splitting in the VB of tb-MnSe can be attributed to the in-plane orbitals, which have wave functions segregated on different z planes and, as a result, are more susceptible to the \mathcal{E}_z . In addition, tunability in electronic states can be achieved by the strain engineering of 2D materials [66]. The in-plane biaxial strain preserves the crystal symmetry, thus creating no additional splittings. However, the strength of NRSS (α) around K_c/M_c for twisted bilayers is modified under biaxial in-plane strain [Fig. 5(d)]. α increases with compressive strain and decreases with tensile strain, providing exceptional tunability.

Similar effects were also investigated for other twist angles, including 9.43°, 13.17°, 27.79°, 32.20°, 38.21°, and 42.10° (see Sec. IV of the SM [48]). The δE also depends upon the dispersiveness of energy bands, where δE increases with increasing band dispersion. The linear NRSS is more prominent for the twist angles around 30°, as the structure deviates from the \mathcal{PT} -symmetric ($\theta = 0^\circ, 60^\circ$) counterparts by the highest amount. In addition, the strength of splitting is the same for twist angles θ and $60^\circ - \theta$ (see Sec. V of the SM [48]). MnPSe₃ and MnSe contain relatively lighter elements with negligible SOC effects (see Sec. VI of the SM [48]). The Zeeman splitting observed in bilayer MnSe with a twist angle of $\theta = 0^\circ$ is ~ 180 meV under 10 MV/cm of the vertical electric field [30], nearly similar to 21.79° tb-MnSe of ~ 175 meV with the same electric field. Similarly, the Zeeman effect in 0° tb-MnPSe₃ is negligible [29], like 21.79° tb-MnPSe₃. Therefore, the order of Zeeman spin splitting depends much on how opposite spin sublattices are arranged in the monolayer concerning the electric field and has less to do with the twist angle. Note that the models in this study include only spin degrees of freedom, thus revealing spin splitting qualitatively. For quantitative analysis, other degrees of freedom (i.e., orbital and sublattice) through first-principles or multiband tight-binding model calculations need to be included.

To summarize, we have shown that NRSS can be induced in 2D \mathcal{PT} -symmetric antiferromagnets by taking bilayers with a relative twist. By first-principles calculations and symmetry analysis, we further predict spin-moment coupling in

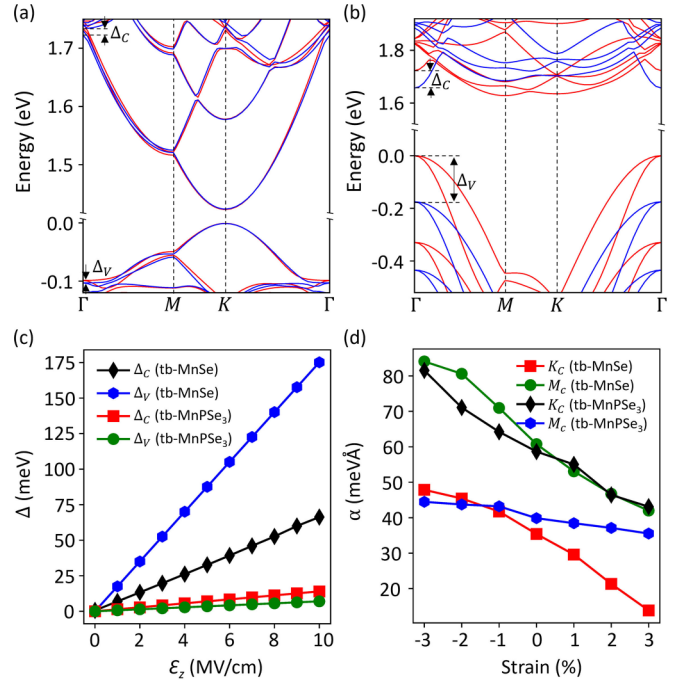


FIG. 5. Band structures of 21.79° (a) tb-MnPSe₃ and (b) tb-MnSe in the presence of the out-of-plane electric field (\mathcal{E}_z) of strength 10 MV/cm. (c) The Zeeman spin splittings in the CB (Δ_C) and VB (Δ_V) of 21.79° tb-MnPSe₃ and tb-MnSe at Γ point as a function of \mathcal{E}_z . (d) The variation in α [see Eq. (1)] as a function of biaxial strain for 21.79° tb-MnPSe₃ and tb-MnSe.

21.79° tb-MnPSe₃ and tb-MnSe that accommodate linear NRSS as large as ~ 90 meV Å. The lateral electric field splits otherwise spin-degenerate bands along the HSPs through magnetoelectric coupling, with more prominent effects in tb-MnSe. In addition, NRSSs are tunable using the biaxial strain. The measurement of these spin splittings can be conducted through well-established optical [29] and electrical transport [69] techniques commonly used in the field of spintronics. Employing antiferromagnets featuring spin-split bands as described in the present study may obviate the necessity for a heavy-metal layer, given that the current AFM mechanism yields a substantial magnitude of spin-moment splitting, even with lighter elements. Moreover, the low-Z antiferromagnets with even larger NRSSs can be predicted by the inverse design approach with desired functionality [70]. In addition, NRSS in moiré-induced flat bands ($\theta \lesssim 3^\circ$) can be an interesting avenue to prospect. We aspire to broaden the pool of available materials and enrich the field of AFM semiconductor spintronics [1,2] through the complete realization of original devices.

S.S. acknowledges CSIR, India, for support from a senior research fellowship [Grant No. 09/086(1432)/2019-EMR-I]. S.B. acknowledges financial support from SERB under a core research grant (Grant No. CRG/2019/000647) to set up high-performance computing facility “Veena” at IIT Delhi for computational resources.

- [1] I. Žutić, J. Fabian, and S. D. Sarma, Spintronics: Fundamentals and applications, *Rev. Mod. Phys.* **76**, 323 (2004).
- [2] A. Fert, Nobel lecture: Origin, development, and future of spintronics, *Rev. Mod. Phys.* **80**, 1517 (2008).
- [3] G. Dresselhaus, Spin-orbit coupling effects in zinc blende structures, *Phys. Rev.* **100**, 580 (1955).
- [4] E. Rashba, Properties of semiconductors with an extremum loop. I. Cyclotron and combination resonance in a magnetic field perpendicular to the plane of the loop, *Sov. Phys. Solid State* **2**, 1109 (1960).
- [5] F. Vas'ko, Spin splitting in the spectrum of two-dimensional electrons due to the surface potential, *JETP Lett.* **30**, 541 (1979).
- [6] Y. A. Bychkov and É. I. Rashba, Properties of a 2D electron gas with lifted spectral degeneracy, *JETP Lett.* **39**, 78 (1984).
- [7] A. F. Young, C. R. Dean, L. Wang, H. Ren, P. Cadden-Zimansky, K. Watanabe, T. Taniguchi, J. Hone, K. L. Shepard, and P. Kim, Spin and valley quantum Hall ferromagnetism in graphene, *Nat. Phys.* **8**, 550 (2012).
- [8] C. Ciccarelli, L. Anderson, V. Tshitoyan, A. Ferguson, F. Gerhard, C. Gould, L. Molenkamp, J. Gayles, J. Železný, L. Šmejkal *et al.*, Room-temperature spin-orbit torque in NiMnSb, *Nat. Phys.* **12**, 855 (2016).
- [9] R. J. Elliott, Theory of the effect of spin-orbit coupling on magnetic resonance in some semiconductors, *Phys. Rev.* **96**, 266 (1954).
- [10] F. Seitz, D. Turnbull, and H. Ehrenreich, *Solid State Physics* (Academic Press, 1968).
- [11] M. Dyakonov and V. Perel, Spin relaxation of conduction electrons in noncentrosymmetric semiconductors, *Sov. Phys. Solid State* **13**, 3023 (1972).
- [12] J. Han, R. Cheng, L. Liu, H. Ohno, and S. Fukami, Coherent antiferromagnetic spintronics, *Nat. Mater.* **22**, 684 (2023).
- [13] V. Baltz, A. Manchon, M. Tsoi, T. Moriyama, T. Ono, and Y. Tserkovnyak, Antiferromagnetic spintronics, *Rev. Mod. Phys.* **90**, 015005 (2018).
- [14] T. Jungwirth, X. Marti, P. Wadley, and J. Wunderlich, Antiferromagnetic spintronics, *Nat. Nanotechnol.* **11**, 231 (2016).
- [15] T. Jungwirth, J. Sinova, A. Manchon, X. Marti, J. Wunderlich, and C. Felser, The multiple directions of antiferromagnetic spintronics, *Nat. Phys.* **14**, 200 (2018).
- [16] J. Železný, P. Wadley, K. Olejník, A. Hoffmann, and H. Ohno, Spin transport and spin torque in antiferromagnetic devices, *Nat. Phys.* **14**, 220 (2018).
- [17] S. Pekar and E. Rashba, Combined resonance in crystals in inhomogeneous magnetic fields, *Sov. Phys. JETP* **20**, 1295 (1965).
- [18] L. Šmejkal, J. Sinova, and T. Jungwirth, Beyond conventional ferromagnetism and antiferromagnetism: A phase with nonrelativistic spin and crystal rotation symmetry, *Phys. Rev. X* **12**, 031042 (2022).
- [19] L. Šmejkal, J. Sinova, and T. Jungwirth, Emerging research landscape of altermagnetism, *Phys. Rev. X* **12**, 040501 (2022).
- [20] S. Hayami, Y. Yanagi, and H. Kusunose, Momentum-dependent spin splitting by collinear antiferromagnetic ordering, *J. Phys. Soc. Jpn.* **88**, 123702 (2019).
- [21] L.-D. Yuan, Z. Wang, J.-W. Luo, E. I. Rashba, and A. Zunger, Giant momentum-dependent spin splitting in centrosymmetric low-Z antiferromagnets, *Phys. Rev. B* **102**, 014422 (2020).
- [22] S. Hayami, Y. Yanagi, and H. Kusunose, Bottom-up design of spin-split and reshaped electronic band structures in antiferromagnets without spin-orbit coupling: Procedure on the basis of augmented multipoles, *Phys. Rev. B* **102**, 144441 (2020).
- [23] L.-D. Yuan, Z. Wang, J.-W. Luo, and A. Zunger, Prediction of low-Z collinear and noncollinear antiferromagnetic compounds having momentum-dependent spin splitting even without spin-orbit coupling, *Phys. Rev. Mater.* **5**, 014409 (2021).
- [24] R. González-Hernández, L. Šmejkal, K. Výborný, Y. Yahagi, J. Sinova, T. Jungwirth, and J. Železný, Efficient electrical spin splitter based on nonrelativistic collinear antiferromagnetism, *Phys. Rev. Lett.* **126**, 127701 (2021).
- [25] L. Šmejkal, A. B. Hellenes, R. González-Hernández, J. Sinova, and T. Jungwirth, Giant and tunneling magnetoresistance in unconventional collinear antiferromagnets with nonrelativistic spin-momentum coupling, *Phys. Rev. X* **12**, 011028 (2022).
- [26] L.-D. Yuan and A. Zunger, Degeneracy removal of spin bands in collinear antiferromagnets with non-interconvertible spin-structure motif pair, *Adv. Mater.* **35**, 2211966 (2023).
- [27] P. Dufek, K. Schwarz, and P. Blaha, Electronic and magnetic structure of MnF₂ and NiF₂, *Phys. Rev. B* **48**, 12672 (1993).
- [28] T. Maitra and R. Valenti, Orbital order in ZnV₂O₄, *Phys. Rev. Lett.* **99**, 126401 (2007).
- [29] N. Sivasdas, S. Okamoto, and D. Xiao, Gate-controllable magneto-optic Kerr effect in layered collinear antiferromagnets, *Phys. Rev. Lett.* **117**, 267203 (2016).
- [30] S. Sheoran and S. Bhattacharya, Multiple Zeeman-type hidden spin splittings in \mathcal{PT} -symmetric layered antiferromagnets, *Phys. Rev. B* **109**, L020404 (2024).
- [31] H. J. Zhao, X. Liu, Y. Wang, Y. Yang, L. Bellaiche, and Y. Ma, Zeeman effect in centrosymmetric antiferromagnetic semiconductors controlled by an electric field, *Phys. Rev. Lett.* **129**, 187602 (2022).
- [32] R. He, D. Wang, N. Luo, J. Zeng, K.-Q. Chen, and L.-M. Tang, Nonrelativistic spin-momentum coupling in antiferromagnetic twisted bilayers, *Phys. Rev. Lett.* **130**, 046401 (2023).
- [33] L.-D. Yuan, X. Zhang, C. M. Acosta, and A. Zunger, Uncovering spin-orbit coupling-independent hidden spin polarization of energy bands in antiferromagnets, *Nat. Commun.* **14**, 5301 (2023).
- [34] R. Basnet, K. M. Kotur, M. Rybak, C. Stephenson, S. Bishop, C. Autieri, M. Birowska, and J. Hu, Controlling magnetic exchange and anisotropy by nonmagnetic ligand substitution in layered MPX₃ ($M = \text{Ni, Mn}$; $X = \text{S, Se}$), *Phys. Rev. Res.* **4**, 023256 (2022).
- [35] C. Autieri, G. Cuono, C. Noce, M. Rybak, K. M. Kotur, C. E. Agrapidis, K. Wohlfeld, and M. Birowska, Limited ferromagnetic interactions in monolayers of MPS₃ ($M = \text{Mn and Ni}$), *J. Phys. Chem. C* **126**, 6791 (2022).
- [36] N. Pournaghavi, M. F. Islam, R. Islam, C. Autieri, T. Dietl, and C. M. Canali, Realization of the Chern-insulator and axion-insulator phases in antiferromagnetic MnTe/Bi₂(Se, Te)₃/MnTe heterostructures, *Phys. Rev. B* **103**, 195308 (2021).
- [37] M. Aapro, M. N. Huda, J. Karthikeyan, S. Kezilebieke, S. C. Ganguli, H. G. Herrero, X. Huang, P. Liljeroth, and H.-P. Komsa, Synthesis and properties of monolayer MnSe with unusual atomic structure and antiferromagnetic ordering, *ACS Nano* **15**, 13794 (2021).
- [38] S. Sattar, M. F. Islam, and C. M. Canali, Monolayer MnX and Janus XMnY ($X, Y = \text{S, Se, Te}$): A family of two-dimensional

- antiferromagnetic semiconductors, *Phys. Rev. B* **106**, 085410 (2022).
- [39] Y.-F. Zhao, L.-J. Zhou, F. Wang, G. Wang, T. Song, D. Ovchinnikov, H. Yi, R. Mei, K. Wang, M. H. Chan *et al.*, Even-odd layer-dependent anomalous Hall effect in topological magnet MnBi_2Te_4 thin films, *Nano Lett.* **21**, 7691 (2021).
- [40] N. Sivadas, S. Okamoto, X. Xu, C. J. Fennie, and D. Xiao, Stacking-dependent magnetism in bilayer CrI_3 , *Nano Lett.* **18**, 7658 (2018).
- [41] K. Lee, A. H. Dismukes, E. J. Telford, R. A. Wiscons, J. Wang, X. Xu, C. Nuckolls, C. R. Dean, X. Roy, and X. Zhu, Magnetic order and symmetry in the 2D semiconductor CrSBr , *Nano Lett.* **21**, 3511 (2021).
- [42] W. Brinkman and R. J. Elliott, Theory of spin-space groups, *Proc. R. Soc. London A* **294**, 343 (1966).
- [43] D. B. Litvin and W. Opechowski, Spin groups, *Physica* **76**, 538 (1974).
- [44] D. B. Litvin, Spin point groups, *Acta Cryst. A* **33**, 279 (1977).
- [45] P. Liu, J. Li, J. Han, X. Wan, and Q. Liu, Spin-group symmetry in magnetic materials with negligible spin-orbit coupling, *Phys. Rev. X* **12**, 021016 (2022).
- [46] G. Kresse and D. Joubert, From ultrasoft pseudopotentials to the projector augmented-wave method, *Phys. Rev. B* **59**, 1758 (1999).
- [47] G. Kresse and J. Furthmüller, Efficient iterative schemes for *ab initio* total-energy calculations using a plane-wave basis set, *Phys. Rev. B* **54**, 11169 (1996).
- [48] See Supplemental Material at <http://link.aps.org/supplemental/10.1103/PhysRevMaterials.8.L051401> for computational methods, symmetry analysis of monolayer, bilayer, and twisted bilayers, results for twist angles other than 21.79° , correlation between twist angle θ and $60^\circ - \theta$, and effect of spin-orbit coupling. The Supplemental Material also includes Refs. [18,21,29,30,46,47,49,51,64,67,71–89].
- [49] M. S. Dresselhaus, G. Dresselhaus, and A. Jorio, *Group Theory: Application to the Physics of Condensed Matter* (Springer Science & Business Media, 2007).
- [50] K. Uchida, S. Furuya, J.-I. Iwata, and A. Oshiyama, Atomic corrugation and electron localization due to moiré patterns in twisted bilayer graphenes, *Phys. Rev. B* **90**, 155451 (2014).
- [51] J. S. B. Lopes dos Santos, N. M. R. Peres, and A. H. Castro Neto, Graphene bilayer with a twist: Electronic structure, *Phys. Rev. Lett.* **99**, 256802 (2007).
- [52] H. Jafari, E. Barts, P. Przybysz, K. Tenzin, P. J. Kowalczyk, P. Dabrowski, and J. Sławińska, Robust Zeeman-type band splitting in sliding ferroelectrics, *Phys. Rev. Mater.* **8**, 024005 (2024).
- [53] S. Sheoran, M. Jain, R. Moulik, and S. Bhattacharya, Probing the uniaxial strain-dependent valley drift and Berry curvature in monolayer MoSi_2N_4 , *Phys. Rev. Mater.* **7**, 114003 (2023).
- [54] S. Sheoran, A. Phutela, R. Moulik, and S. Bhattacharya, Manipulation of valley and spin properties in two-dimensional Janus WSiGeZ_4 ($Z = \text{N, P, As}$) through symmetry control, *J. Phys. Chem. C* **127**, 11396 (2023).
- [55] H. J. Zhao, H. Nakamura, R. Arras, C. Paillard, P. Chen, J. Gosteau, X. Li, Y. Yang, and L. Bellaïche, Purely cubic spin splittings with persistent spin textures, *Phys. Rev. Lett.* **125**, 216405 (2020).
- [56] L. Tao and E. Y. Tsymbal, Persistent spin texture enforced by symmetry, *Nat. Commun.* **9**, 2763 (2018).
- [57] S. Varotto, A. Johansson, B. Göbel, L. M. Vicente-Arche, S. Mallik, J. Bréhin, R. Salazar, F. Bertran, P. L. Fèvre, N. Bergeal *et al.*, Direct visualization of Rashba-split bands and spin/orbital-charge interconversion at KTaO_3 interfaces, *Nat. Commun.* **13**, 6165 (2022).
- [58] G. J. Omar, W. L. Kong, H. Jani, M. S. Li, J. Zhou, Z. S. Lim, S. Prakash, M. S. Li, S. Hooda, T. Venkatesan *et al.*, Experimental evidence of t_{2g} electron-gas Rashba interaction induced by asymmetric orbital hybridization, *Phys. Rev. Lett.* **129**, 187203 (2022).
- [59] J. Nitta, T. Akazaki, H. Takayanagi, and T. Enoki, Gate control of spin-orbit interaction in an inverted $\text{In}_{0.53}\text{Ga}_{0.47}\text{As}/\text{In}_{0.52}\text{Al}_{0.48}\text{As}$ heterostructure, *Phys. Rev. Lett.* **78**, 1335 (1997).
- [60] T. Hu, F. Jia, G. Zhao, J. Wu, A. Stroppa, and W. Ren, Intrinsic and anisotropic Rashba spin splitting in Janus transition-metal dichalcogenide monolayers, *Phys. Rev. B* **97**, 235404 (2018).
- [61] A. Weston, E. G. Castanon, V. Enaldiev, F. Ferreira, S. Bhattacharjee, S. Xu, H. Corte-León, Z. Wu, N. Clark, A. Summerfield *et al.*, Interfacial ferroelectricity in marginally twisted 2D semiconductors, *Nat. Nanotechnol.* **17**, 390 (2022).
- [62] S. Talkington and E. J. Mele, Electric-field-tunable band gap in commensurate twisted bilayer graphene, *Phys. Rev. B* **107**, L041408 (2023).
- [63] S. Sheoran, S. Monga, A. Phutela, and S. Bhattacharya, Coupled spin-valley, Rashba effect, and hidden spin polarization in WSi_2N_4 family, *J. Phys. Chem. Lett.* **14**, 1494 (2023).
- [64] J. Neugebauer and M. Scheffler, Adsorbate-substrate and adsorbate-adsorbate interactions of Na and K adlayers on $\text{Al}(111)$, *Phys. Rev. B* **46**, 16067 (1992).
- [65] M. Fiebig, Revival of the magnetoelectric effect, *J. Phys. D* **38**, R123 (2005).
- [66] Z. Dai, L. Liu, and Z. Zhang, Strain engineering of 2D materials: Issues and opportunities at the interface, *Adv. Mater.* **31**, 1805417 (2019).
- [67] M. H. Naik and M. Jain, Ultraflatbands and shear solitons in moiré patterns of twisted bilayer transition metal dichalcogenides, *Phys. Rev. Lett.* **121**, 266401 (2018).
- [68] L. Xu, H. Liu, C. Song, X. Li, F. Li, D. Li, L. Wang, X. Bai, and J. Qi, Evolution of interlayer stacking orders and rotations in bilayer PtSe_2 visualized by stem, *2D Mater.* **8**, 025014 (2021).
- [69] D.-F. Shao, Y.-Y. Jiang, J. Ding, S.-H. Zhang, Z.-A. Wang, R.-C. Xiao, G. Gurus, W. J. Lu, Y. P. Sun, and E. Y. Tsymbal, Néel spin currents in antiferromagnets, *Phys. Rev. Lett.* **130**, 216702 (2023).
- [70] A. Zunger, Inverse design in search of materials with target functionalities, *Nat. Rev. Chem.* **2**, 0121 (2018).
- [71] J. P. Perdew, K. Burke, and M. Ernzerhof, Generalized gradient approximation made simple, *Phys. Rev. Lett.* **77**, 3865 (1996).
- [72] S. Grimme, Semiempirical GGA-type density functional constructed with a long-range dispersion correction, *J. Comput. Chem.* **27**, 1787 (2006).
- [73] A. I. Liechtenstein, V. I. Anisimov, and J. Zaanen, Density-functional theory and strong interactions: Orbital ordering in Mott-Hubbard insulators, *Phys. Rev. B* **52**, R5467 (1995).

- [74] M. I. Aroyo, J. M. Perez-Mato, C. Capillas, E. Kroumova, S. Ivantchev, G. Madariaga, A. Kirov, and H. Wondratschek, Bilbao crystallographic server: I. Databases and crystallographic computing programs, *Z. Kristallogr. - Cryst. Mater.* **221**, 15 (2006).
- [75] L. Elcoro, B. Bradlyn, Z. Wang, M. G. Vergniory, J. Cano, C. Felser, B. A. Bernevig, D. Orobengoa, G. Flor, and M. I. Aroyo, Double crystallographic groups and their representations on the Bilbao crystallographic server, *J. Appl. Crystallogr.* **50**, 1457 (2017).
- [76] H. T. Stokes and D. M. Hatch, *FINDSYM*: Program for identifying the space-group symmetry of a crystal, *J. Appl. Crystallogr.* **38**, 237 (2005).
- [77] Y. Hinuma, G. Pizzi, Y. Kumagai, F. Oba, and I. Tanaka, Band structure diagram paths based on crystallography, *Comput. Mater. Sci.* **128**, 140 (2017).
- [78] V. Wang, N. Xu, J.-C. Liu, G. Tang, and W.-T. Geng, VASPKIT: A user-friendly interface facilitating high-throughput computing and analysis using VASP code, *Comput. Phys. Commun.* **267**, 108033 (2021).
- [79] U. Herath, P. Tavazde, X. He, E. Bousquet, S. Singh, F. Muñoz, and A. H. Romero, PyProcar: A Python library for electronic structure pre/post-processing, *Comput. Phys. Commun.* **251**, 107080 (2020).
- [80] A. Jain, S. P. Ong, G. Hautier, W. Chen, W. D. Richards, S. Dacek, S. Cholia, D. Gunter, D. Skinner, G. Ceder *et al.*, Commentary: The materials project: A materials genome approach to accelerating materials innovation, *APL Mater.* **1**, 011002 (2013).
- [81] S. V. Gallego, J. M. Perez-Mato, L. Elcoro, E. S. Tasci, R. M. Hanson, K. Momma, M. I. Aroyo, and G. Madariaga, *MAGNDATA*: Towards a database of magnetic structures. I. The commensurate case, *J. Appl. Crystallogr.* **49**, 1750 (2016).
- [82] Mathematica, version 13.3, <https://www.wolfram.com/mathematica>.
- [83] X. Liu, A. P. Pyatakov, and W. Ren, Magnetoelectric coupling in multiferroic bilayer VS₂, *Phys. Rev. Lett.* **125**, 247601 (2020).
- [84] G. Constantinescu, A. Kuc, and T. Heine, Stacking in bulk and bilayer hexagonal boron nitride, *Phys. Rev. Lett.* **111**, 036104 (2013).
- [85] L. Tao and E. Y. Tsybal, Perspectives of spin-textured ferroelectrics, *J. Phys. D* **54**, 113001 (2021).
- [86] S. Calder, A. V. Haglund, A. I. Kolesnikov, and D. Mandrus, Magnetic exchange interactions in the van der Waals layered antiferromagnet MnPSe₃, *Phys. Rev. B* **103**, 024414 (2021).
- [87] M. Milivojević, M. Orozović, S. Picozzi, M. Gmitra, and S. Stavić, Interplay of altermagnetism and weak ferromagnetism in two-dimensional RuF₄, [arXiv:2401.15424](https://arxiv.org/abs/2401.15424).
- [88] T. Adamantopoulos, M. Merte, F. Freimuth, D. Go, M. Ležaić, W. Feng, Y. Yao, J. Sinova, L. Šmejkal, S. Blügel *et al.*, Spin and orbital magnetism by light in rutile altermagnets, [arXiv:2403.10235](https://arxiv.org/abs/2403.10235).
- [89] S. Bhowal and N. A. Spaldin, Ferroically ordered magnetic octupoles in *d*-wave altermagnets, *Phys. Rev. X* **14**, 011019 (2024).